Check for updates 15214095, 2022, 12, Downloaded from https://onlinelibrary.wiley.com/doi/10.1002/adma.2012105023 by UNCL: University Of Nebraska - Line Acquisitions Accounting, Wiley Online Library on [25.01/2023]. See the Terms and Conditions (https://onlinelibrary.wiley.com/doi/) on Wiley Online Library for rules of use C) A stricks are governed by the applicable Centering Commons Library for rules of use C). *A*DVANCED www.advmat.de

Keke He,* Bilal Barut, Shenchu Yin, Michael D. Randle, Ripudaman Dixit, Nargess Arabchigavkani, Jubin Nathawat, Ather Mahmood, Will Echtenkamp, Christian Binek, Peter A. Dowben, and Jonathan P. Bird*

Evidence of robust spin-dependent transport in monolayer graphene, deposited on the (0001) surface of the antiferromagnetic (AFM)/magneto-electric oxide chromia (Cr₂O₃), is provided. Measurements performed in the non-local spin-Hall geometry reveal a robust signal that is present at zero external magnetic field and which is significantly larger than any possible ohmic contribution. The spin-related signal persists well beyond the Néel temperature (≈307 K) that defines the transition between the AFM and paramagnetic states, remaining visible at the highest studied temperature of close to 450 K. This robust character is consistent with prior theoretical studies of the graphene/ Cr₂O₃ system, predicting that the lifting of sub-lattice symmetry in the graphene shall induce an effective spin-orbit term of ≈40 meV. Overall, the results indicate that graphene-on-chromia heterostructures are a highly promising framework for the implementation of spintronic devices, capable of operation well beyond room temperature.

1. Introduction

Spintronic devices^[1-4] have attracted ongoing interest as a means to confront the challenges of continued complementary metal-oxide-semiconductor (CMOS) scaling. Graphene has been widely discussed for such applications, having long spin-relaxation lengths that make it well suited for use in spin-transistor geometries.^[5-9] Recent studies of commercialgrade graphene, grown by chemical vapor deposition (CVD), have demonstrated spin-diffusion lengths in excess of 10 µm at room temperature,[10-12] a result that points to the huge

K. He, B. Barut, S. Yin, M. D. Randle, R. Dixit, N. Arabchigavkani, J. Nathawat, J. P. Bird Department of Electrical Engineering University at Buffalo The State University of New York Buffalo, New York 14260, USA E-mail: kekehe@buffalo.edu; jbird@buffalo.edu A. Mahmood, W. Echtenkamp, C. Binek, P. A. Dowben Department of Physics and Astronomy Theodore Jorgensen Hall University of Nebraska Lincoln Lincoln, Nebraska 68588-0299, USA

The ORCID identification number(s) for the author(s) of this article can be found under https://doi.org/10.1002/adma.202105023.

DOI: 10.1002/adma.202105023

potential of this 2D material for spintronic applications. The weak spin relaxation in graphene can be ascribed to its vanishingly small native spin-orbit coupling^[13–16] (SOC), a property that makes the manipulation of spins in the same material challenging.[4] To resolve this conundrum, various strategies have been explored to introduce magnetic character into graphene, most notably by exploiting proximity effects at its interface with an appropriate magnetic substrate.[17-24] The development of functional room-temperature devices based upon such heterostructures remains an ongoing challenge.

Another approach to enhancing SOC in graphene relies on breaking the sublattice symmetry of its pristine crystal.[25,26] By opening a gap between the conduction and valence bands, this distortion effec-

tively adds a SOC term to the Hamiltonian of graphene. In one such approach, hydrogenation has been used to induce sp²-to-sp³ bond conversion, causing a buckling of the graphene structure that yields clear signatures of spin transport at room temperature. [27] Symmetry breaking has also been achieved by supporting graphene on a variety of non-magnetic substrates, such as SiC, [28] Al₂O₃,^[29] MgO,^[30] and BN.^[31] While these approaches have their advantages, none of them offer the non-volatility desired to imbue spintronic devices with a potential edge over CMOS.^[32]

Herein, we describe an approach to achieving robust spindependent transport in graphene, well beyond room temperature, that we realize by supporting this two-dimensional material on a substrate comprised of an antiferromagnetic (AFM) oxide (chromia, Cr2O3). One of a small number of materials to exhibit magneto-electric (ME) nature (i.e., coupling of magnetic and electrostatic polarizations) at room temperature (and beyond),[33,34] chromia is antiferromagnetic (AFM) in bulk but exhibits a net alignment of magnetic moments at its (0001) surface.[33,35-37] This boundary magnetism allows chromia to function as a highly spin-polarized substrate, which is ideally suited for combination with a graphene overlayer. [32,38] The excellent dielectric character^[39,40] of chromia, along with its ME nature, allows an applied voltage to be used to reverse the direction of its boundary magnetization, at significantly lower energy cost (≈aJ) than that associated with the current-driven switching of ferromagnets.[32]

We fabricated graphene transistors on (0001) Cr₂O₃ substrates, demonstrating non-local Hall signals^[27] that provide a clear indication of induced spin transport. When the chromia is prepared in a single ME domain, [36] at temperatures below its Néel temperature ($T_N \approx 307$ K), the non-local signal exhibits clear indications of the ME character of the chromia. The spin signal is also found to persist well beyond T_N , where any boundary magnetism should be lost, remaining visible at the highest studied temperature of ≈450 K. These observations are consistent with the results of prior theoretical work, which predict that chromia breaks the crystal symmetry of graphene (from C_{6v} to C_{3v}) and generates an effective SOC term of ≈40 meV.^[25,26,41] As such, our observations point to the suitability of chromia/graphene heterostructures for use in spintronic devices, capable of operation at room temperature and beyond. [26,42] This should be contrasted with prior studies of proximity effects in graphene/AFM heterolayers;[24,43-45] while some of these works^[24,45] have established the presence of very large exchange coupling between the layers, this situation is only realized for temperatures below T_N . In our case, however, as the origin of the inferred SOC is fundamentally structural in nature, the spin transport is able to persist well beyond the critical temperature of the antiferromagnet.

2. Results and Discussion

The essential principle of our experiments is indicated in the schematic of Figure 1a. Here, we indicate the spin currents that arise in a graphene layer, in the presence of external SOC generated at the (0001) Cr₂O₃ surface. The manner in which we realize this system in practice is indicated in Figure 1b, which shows an electron microscopy image of one of the devices that we have fabricated. To confirm the presence of the nonzero boundary magnetism in our Cr₂O₃ films (whose structural properties are characterized in Section S1, Supporting Information) below T_N , we also fabricated 3.7 nm-thick Pt Hall bars on their (0001) surface. Nonmagnetic heavy metals have recently been used to detect the boundary magnetization of chromia.[46-48] In the case of Pt, the resulting signal is widely believed to originate from spin-Hall magneto-resistance, associated with an imaginary component in the mixing conductance. [49,50] In Figure 1c, we plot the temperature-dependent resistance of one of our Pt Hall bars. These (local Hall) measurements were performed by following a procedure in which the Pt/Cr₂O₃ system was first warmed to 330 K, thereby causing the chromia to transition from an antiferromagnet to a paramagnet. Next, the sample was prepared in a particular ME state by cooling back down below T_N , in the presence of a perpendicular magnetic field of ±3 T (but with no applied gate voltage). After removing this field at 280 K, the data of Figure 1c were then obtained by measuring the zero-field (anomalous) Hall signal while warming up through T_N . Referring to the data shown in this figure, it is clear that two distinct Hall signals are obtained below ≈310 K, consistent with the known^[48] Néel temperature of the films ($T_N \approx 307$ K), and that these signals collapse upon one another when the system is warmed above this critical temperature. This result is consistent with the presence of two oppositely directed AFM states below T_N , associated with which are two distinct configurations of the boundary magnetization.^[37,51] These results therefore confirm that the magnetic properties associated with bulk chromia crystals are preserved in our thin films. (In Section S2 (Supporting Information), we present a further characterization of the boundary magnetism.)

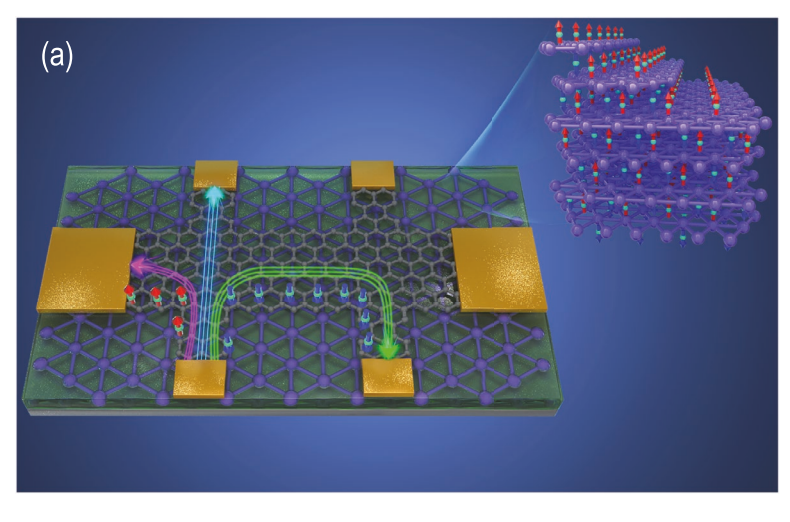
In Figure 1d, we plot the small-signal resistance (R_{local}) as a function of back-gate voltage (V_g) for the eight different devices we studied. (These measurements were performed in a twoprobe geometry, in which current was passed, and the resulting voltage drop was measured, between probes C1 and C2 of Figure 1b.) The minimum in the current that denotes the Dirac point is shifted to positive gate voltage (0 V < V_{o} < 5 V) in each of the devices, implying a p-type doping of the graphene due to its contact with the chromia. Table 1 indicates some key properties from the devices, including (in the bottom row) the (valence band) Fermi-level shift ($\Delta E_{\rm F}$ at $V_{\rm g}=0$ V) due to this doping. [$\Delta E_{\rm F}$ was calculated from the usual expression for the Fermi level in graphene, $E_{\rm F} = \pm \hbar v_{\rm F} (\pi n)^{1/2}$, where *n* is the areal carrier density and the positive (negative) sign applies to the case of net electron (hole) density. The concentration was calculated from the expression $n(V_g) = |(V_g - V_D)C'_{ox}/e|$, where V_D is the value of the gate voltage at the Dirac point and C'ox is the areal capacitance of the back-gate. Given the dielectric constant of chromia $(\varepsilon_{\rm r}=13)$, [40] this parameter takes values of $C'_{\rm ox}=1.15\times 10^{-7}$ and 4.60×10^{-8} F cm⁻², respectively, for the 100 nm- and 250 nm-thick chromia films.] According to Table 1, $\Delta E_{\rm F}$ was in the range of ≈50–200 meV, being systematically smaller for the three devices formed on the thicker chromia (we speculate that this might be due to different surface roughness in the thick and thin films, impacting the contact with the graphene). Hole doping of graphene-on-chromia has been predicted on the basis of density functional theory, which shows that the formation of the heterostructure is accompanied by the transfer of 0.0008 electrons per carbon atom to chromia. [26] For monolayer graphene, this doping level corresponds to $\Delta E_{\rm F} \approx 200$ meV, in reasonable agreement with the numbers quoted in Table 1.

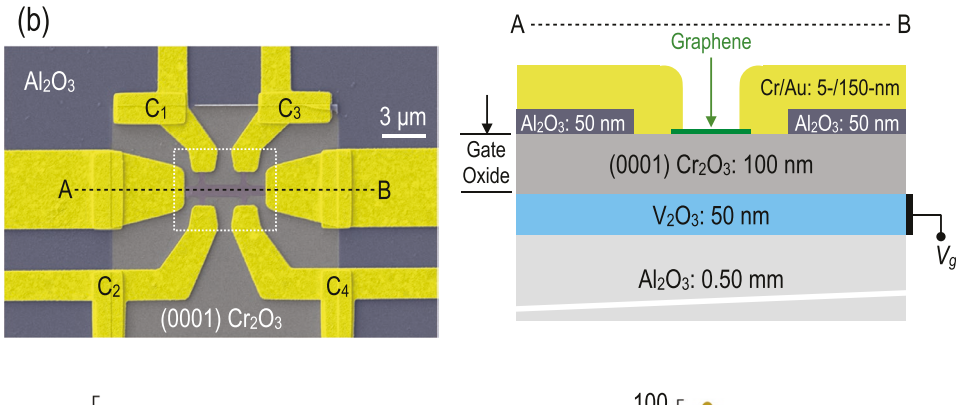
It is apparent from the results of Figure 1d, and from the associated data in Table 1, that considerable variations in mobility were obtained between different devices. While chromia grown on V_2O_3 is known to exhibit excellent dielectric character, its (0001) surface nonetheless exhibits small crystalline grains on the scale of $\approx 50-100$ nm. Although the magnetic properties of this surface are largely insensitive to the presence of these grains, all they can be expected to impact charge transport in a graphene overlayer. We therefore suspect that the mobility variations exhibited by our devices arise from microscopic variations in the structure of the chromia surface, and the impact that these have on adhesion of the graphene and the transport of its charges.

In Figure 2a, we show representative measurements of the non-local resistance ($R_{\rm nl}$) of one of our devices as a function of $V_{\rm g}$ and at various (out of-plane) magnetic fields. In these measurements, a fixed voltage ($V_{\rm d}$) was used to pass a current ($I_{\rm d}$) between probes C_1 and C_2 in Figure 1b; the resulting non-local voltage ($V_{\rm nl}$) that developed between probes C_3 and C_4 was then used to calculate $R_{\rm nl}$ ($\equiv V_{\rm nl}/I_{\rm nl}$). The measurements were made at a fixed temperature of 290 K, after cooling down below $T_{\rm N}$ in the simultaneous presence of static magnetic (6.9 T) and electric (250 kV cm $^{-1}$) fields (both applied normal to the Cr_2O_3 film).

www.advancedsciencenews.com

www.advmat.de





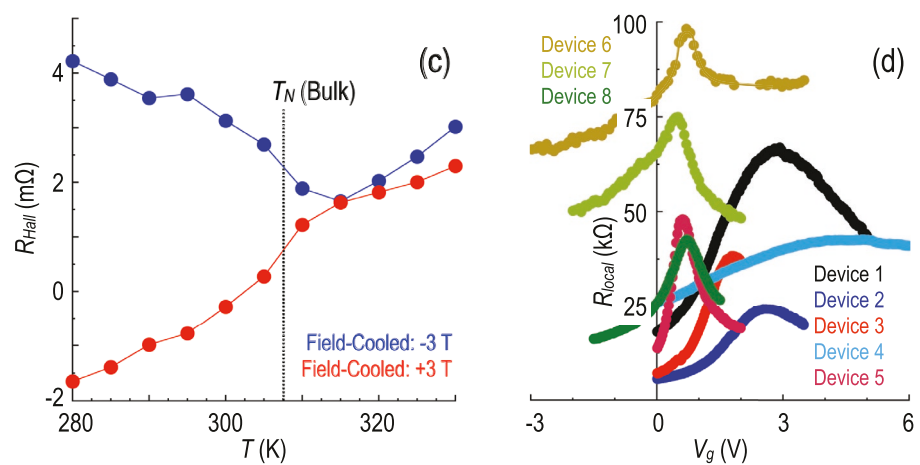


Figure 1. a) Schematic illustrating the main features of our experiment, in which a graphene Hall bar with multiple contacts is formed on (0001) Cr_2O_3 . When a current (blue line with arrow) is driven from the lower to the upper contact on the left, SOC generated by the Cr_2O_3 causes spin separation in graphene, allowing a non-local spin-Hall signal to be detected at the probes to the right. The inset in the upper-right corner represents the magnetic moments (red and blue) in Cr_2O_3 below T_N . The material is AFM in bulk but its (0001) surfaces show non-zero magnetism. b) Shown left is a colorized electron microscopy image of an actual device (Device 4, Cr_2O_3 thickness: 100 nm). The graphene Hall bar is at the center of the area enclosed by the white dotted line. The non-local measurements are made using probes C_1 — C_4 . The schematic on the right represents (not to scale) the layer structure along the line AB in the left image. The contact scheme for gating the device is also indicated. c) Variation of Hall resistance with temperature for a Pt Hall bar fabricated on 100 nm-thick (0001) Cr_2O_3 . Measurements were made under the conditions described in the main text. The dotted line denotes T_N of crystalline, bulk Cr_2O_3 . d) Room-temperature transfer curves of the different devices studied here. The small-signal local resistance (R_{local}) was measured using probes C_1 and C_2 in (b).

Referring to this figure, $R_{\rm nl}$ exhibits a peak at each magnetic field that occurs as the Fermi level moves from the valence to the conduction band. This is confirmed by the behavior shown

in the inset of Figure 2a, which plots the variation of $I_{\rm d}$ for the same range of gate voltage and the same sequence of magnetic fields. The minimum in $I_{\rm d}$, associated with the band crossing

1521495, 2022, 12, Downloaded from https://onlinelibrary.wiley.com/doi/10.1002/adma.202105023 by UNCL: University Of Nebraska - Line Acquisitions Accounting, Wiley Online Library on [25012023]. See the Terms and Conditions (https://onlinelibrary.wiley.com/term

conditions) on Wiley Online Library for rules of use; OA articles are governed by the applicable Creative Commons License

Table 1. Some key parameters for the different devices studied here. L is the separation between the non-local Hall probes and the current probes, e.g., the distance between C_1 and C_3 in Figure 1b. W is the etched width of the graphene Hall bar. The mobility was determined from the room-temperature transfer curves of the devices, with the figures quoted here being obtained by averaging the minimum values of mobility observed on the electron and hole sides of the Dirac point (see Section S3, Supporting Information). The Fermi-level shift (ΔE_F) is calculated by assuming a chromia dielectric constant $\varepsilon_r = 13.$ [40]

	Device 1	Device 2	Device 3	Device 4	Device 5	Device 6	Device 7	Device 8
Cr ₂ O ₃ thickness [nm]	100	100	100	100	100	250	250	250
<i>L</i> [μm]	2	4	3	4	2	7.4	7.4	7.4
<i>W</i> [μm]	0.5	2	1	2	0.5	2.7	2.7	2.7
Mobility [cm ² V ⁻¹ s ⁻¹]	526	2166	3434	543	2868	526	1490	5157
$\Delta E_{\rm F}$ [meV]	169	159	132	220	77	52	44	53

in graphene, clearly correlates well to the position of the maximum in $R_{\rm nl}$, at each of the magnetic fields. This is precisely the behavior expected for the spin-Hall signal, whose magnitude is inversely proportional to the charge conductivity of graphene, [52] and points to the presence of extrinsic SOC that arises from the contact with chromia. [41]

To allow comparison with the magnitude of $R_{\rm nl}$, in Figure 2a we also plot the corresponding variation of the ohmic resistance ($R_{\rm Ohmic}$). This latter quantity is essentially the resistance that should be measured at the non-local probes due to leakage of classical current lines from the local measurement setup^[20,24,53–55]

$$R_{\text{Ohmic}} = \left[\left(\frac{\rho_{xx}}{\pi} \right) \ln \left[\frac{\left(\cosh\left(\frac{\pi L}{W}\right) + 1 \right)}{\left(\cosh\left(\frac{\pi L}{W}\right) - 1 \right)} \right] \approx \rho_{xx} e^{-\pi L/W}$$
 (1)

Here, ρ_{xx} is the longitudinal sheet resistivity, L is the separation of the longitudinal probes, and W is the width of the graphene conductor. [56] The first group of terms (enclosed in square brackets) on the right-hand side of this equation is exact, while

the second (exponential) term is an approximation that holds when the conductor is much longer than it is wide (L > W). In our analysis, we calculate R_{Ohmic} using the former, exact form. Comparing R_{nl} and R_{Ohmic} in Figure 2a, we see that the former is much larger than the latter, at all magnetic fields and gate voltages. (Actually, it is likely that we overestimate R_{Ohmic} , as our two-probe measurement of ρ_{xx} includes contact resistance). This is to be contrasted with the behavior observed for graphene-on-SiO₂, in which similar spin transport is not expected. In Figure 2b, we compare the ohmic and non-local signatures generated in this system. Both $R_{\rm nl}$ and $R_{\rm Ohmic}$ are very much smaller than for graphene-on-chromia, reflecting the weakness of any non-local effect. In addition, their values are similar over the entire range of the measurement, in marked contrast to the results of Figure 2a and consistent with the absence of any significant spin transport in graphene-on-SiO₂.

In the inset to Figure 2b, we plot the non-local signal obtained in measurements of graphene-on-chromia at 270 K and at three different driving voltages (V_d). Even as this bias is increased from 10 to 100 mV, and the dissipated electrical power is increased by a factor of a hundred, we observe no significant influence on $R_{\rm nl}$. On the basis of this observation, we

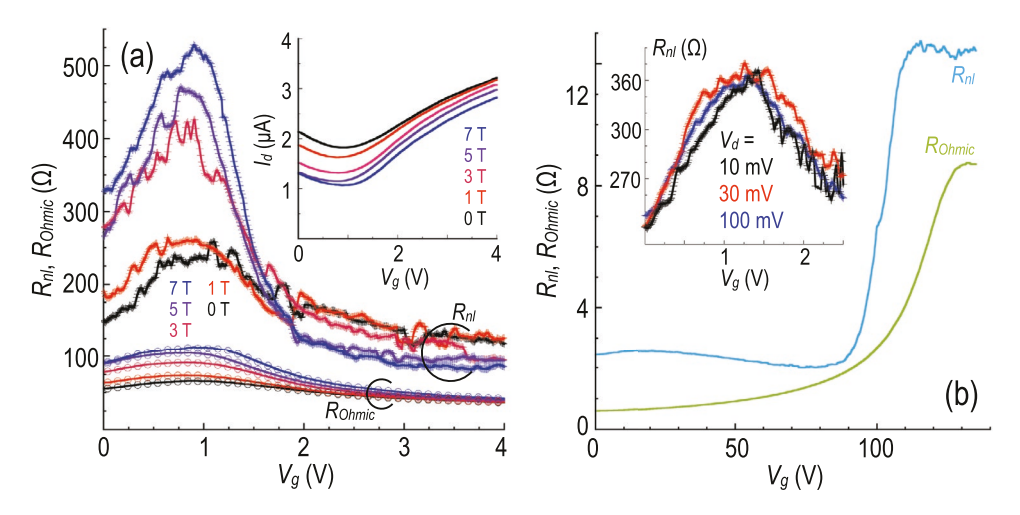


Figure 2. a) The main panel plots the variation of R_{nl} (lines with crosses) and R_{Ohmic} (lines with open circles) at various out-of-plane magnetic fields (indicated). The inset shows the corresponding variation of I_{d} , measured in the local configuration. Measurements were performed on Device 4 at 290 K, after the field-cooling procedure described in the main text. b) The main panel plots the variation of R_{nl} and R_{ohmic} at zero magnetic field and 295 K, for a graphene-on-SiO₂ device. R_{nl} and R_{ohmic} are very similar over the entire range of gate voltage. The inset plots the measured variation of R_{nl} in Device 4 for various source voltages, V_d .

15214095, 2022, 12, Downloaded from https://onlinelibrary.wiley.com/doi/10.1002/adma.202105023 by UNCL: University Of Nebraska

Accounting, Wiley Online Library on [25/01/2023]. See the Terms and Conditions (https://onlinelibrary.wiley.com/terms

and-conditions) on Wiley Online Library for rules of use; OA articles are governed by the applicable Creative Commons License

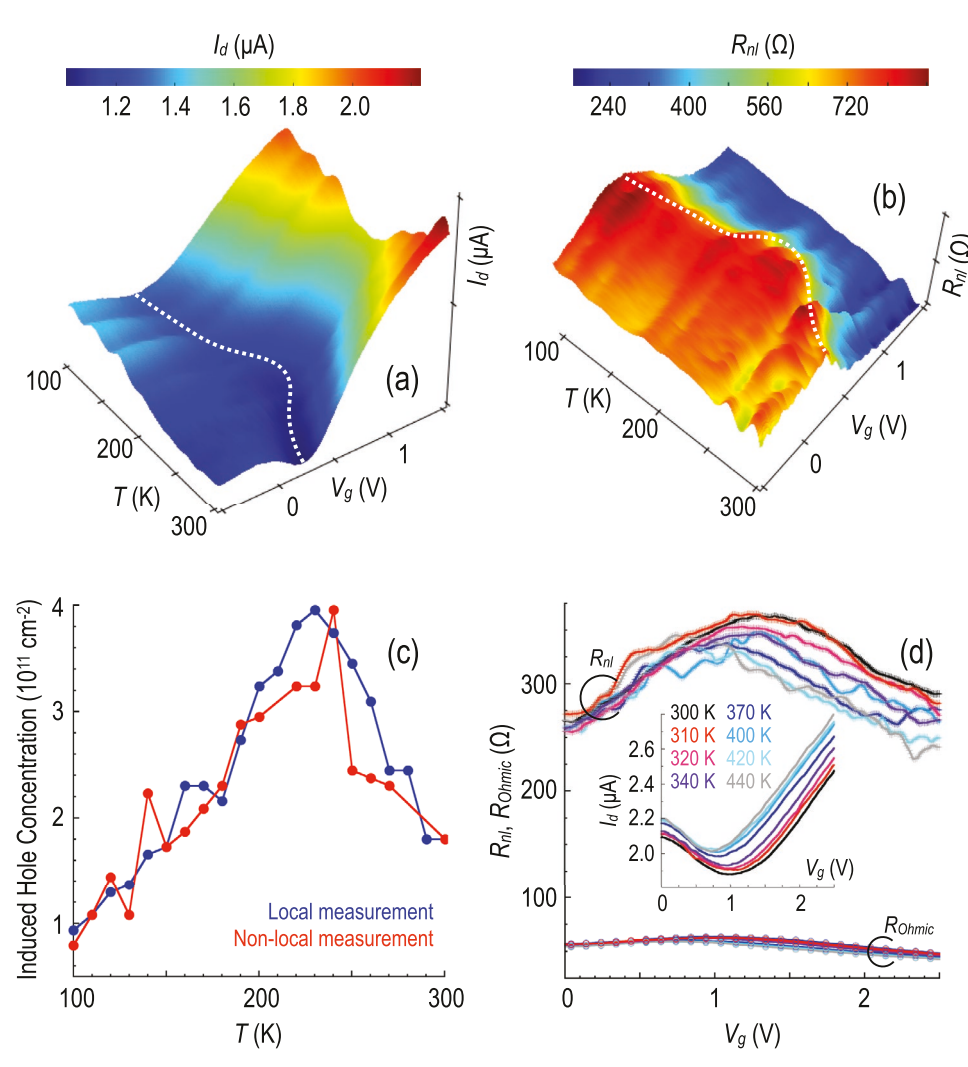


Figure 3. a) $I_d(V_g, T)$, with the white dotted line following the variation of the current minimum that represents the Dirac point. b) Corresponding variation of $R_{nl}(V_g, T)$, where the white dotted line now denotes the position of the maximum in the non-local resistance. c) Induced hole density at the gate voltage corresponding to the minimum in $I_d(V_g, T)$ (blue data) and the maximum in $R_{nl}(V_g, T)$ (red data). (a)–(c) were obtained for Device 4 while warming from 100 K in a magnetic field of 6.9 T, and after first field-cooling from 350 K. d) The main panel plots the variation of R_{nl} (lines with crosses) and R_{Ohmic} (lines with open circles), measured for Device 4 at various temperatures (indicated) above T_N . The inset shows the corresponding variation of I_d , measured in the local configuration.

are able to exclude Joule heating as a possible origin of the non-local signal in Figure 2a.^[54] We also performed in situ energy-dispersive X-ray spectroscopy of our transferred graphene, confirming the absence of any remnant copper on the CVD-grown graphene (see Section S3, Supporting Information). This allows us to exclude copper clusters as the origin of the observed spin-Hall signal.^[56]

The influence of temperature on the non-local spin signal is summarized in the various panels of **Figure 3**. Figure 3a–c concerns measurements obtained while warming a device from 100 to 300 K (i.e., for $T < T_N$), in the presence of an applied magnetic field of 6.9 T. The data were obtained after first field-cooling the device through T_N (as described for Figure 1c), to realize a well-defined ME domain. Figure 3a plots the variation of $I_d(V_g, T)$, with the white dotted line following the variation of the current minimum that defines the Dirac point. In Figure 3b, we plot the corresponding variation of $R_{nl}(V_g, T)$

over the same parameter space, with the white dotted line now indicating the peak value of $R_{\rm nl}$. As expected for the spin-Hall effect, we see that this maximum closely tracks the minimum in the local current, a point that is confirmed quantitatively in Figure 3c; this plots the induced hole doping as calculated from the minimum in $I_{\rm d}$, and the peak in $R_{\rm nl}$, confirming the connection of these quantities to one another. As for the non-monotonic evolution of the induced hole concentration with temperature, evidenced by both data sets, we return to address this shortly below.

Figure 3d addresses the evolution of the non-local signal above $T_{\rm N}$, a point that is crucial to assessing the contributions of structurally induced SOC and proximity-induced magnetic exchange to $R_{\rm nl}$. In these experiments, the temperature is increased from just below $T_{\rm N}$ (300 K) to well above it (440 K), allowing the following observations to be made. First, no dramatic change in the non-local signal occurs when the temperature is

15214095, 2022, 12, Downloaded from https://olimielthtary.wiley.com/doi/10.1002/adma.202105023 by UNCL: University Of Nebraska - Line Acquisitions Accounting, Wiley Online Library on [25012023]. See the Terms and Conditions (https://olimielthtary.wiley.

onditions) on Wiley Online Library for rules of use; OA articles are governed by the applicable Creative Commons License

raised through $T_{\rm N}$ (compare the data at 300, 310, and 320 K), and the non-local resistance instead decays only slowly as the temperature is increased to 440 K. Second, the maximum in $R_{\rm nl}$ follows the minimum of $I_{\rm d}$ over the entire temperature range (compare the main panel with inset), confirming the connection of the non-local signal to the physics of Dirac carriers. Finally, $R_{\rm nl}$ remains considerably larger than $R_{\rm Ohmic}$ over the entire temperature range (compare the data in the main panel), pointing to the true, non-local, nature of $R_{\rm nl}$.

There are a number of aspects of our findings that merit further discussion. The growth of the non-local resistance with increasing magnetic field, shown in Figure 2a, is reminiscent of previous work that has connected this behavior to the lifting of spin and valley degeneracy in graphene. ^[57] In an important contrast with that work, in which the non-local resistance was found to be vanishingly small in the absence of any external magnetic field, our work demonstrates that $R_{\rm nl}$ can be significant even at zero field. In this sense, our measurements suggest that the spin degeneracy in the graphene-on-chromia system is broken even at zero external field.

The influence of the chromia substrate is further apparent in the measurements of Figure 3c, which shows a non-monotonic evolution of the position of both the Dirac-point minimum in $I_{\rm d}$ and the maximum in $R_{\rm nl}$. This variation is highly reminiscent

of that exhibited by chromia's magnetoelectric coefficient; this quantifies the coupling between its magnetic and electric polarizations and also exhibits a maximum in the range of 250–275 K.^[58] The variation of this parameter with temperature should result in a similar variation of the electric polarization at the chromia surface; this in turn should generate a temperature-dependent gating of the graphene, consistent with the behavior shown in Figure 3c.

The results of Figures 2 and 3 imply that the spin relaxation length (λ_s) should be in the range of a few micrometers at room temperature, a reasonable conclusion for wet-transferred CVD graphene handled by standard processing. This idea is further confirmed by experiments in which key spin-transport parameters were inferred by measuring the non-local resistance $(R_{\rm nl})$ as a function of the measurement-probe separation (L). The devices used in these studies were fabricated by the procedure described in the Experimental Section. In **Figure 4**a, we show the structure of the devices in an optical microscopy image (top), while the precise microstructure of the etched graphene is illustrated in an electron microscopy image (bottom). Theoretically, [52,56] $R_{\rm nl}$ is expected to scale according to

$$\frac{R_{\rm nl}}{\rho_{\rm xx}} = \frac{\gamma^2}{2} \left(\frac{W}{\lambda_{\rm s}}\right) e^{(-L/\lambda_{\rm s})} \tag{2}$$

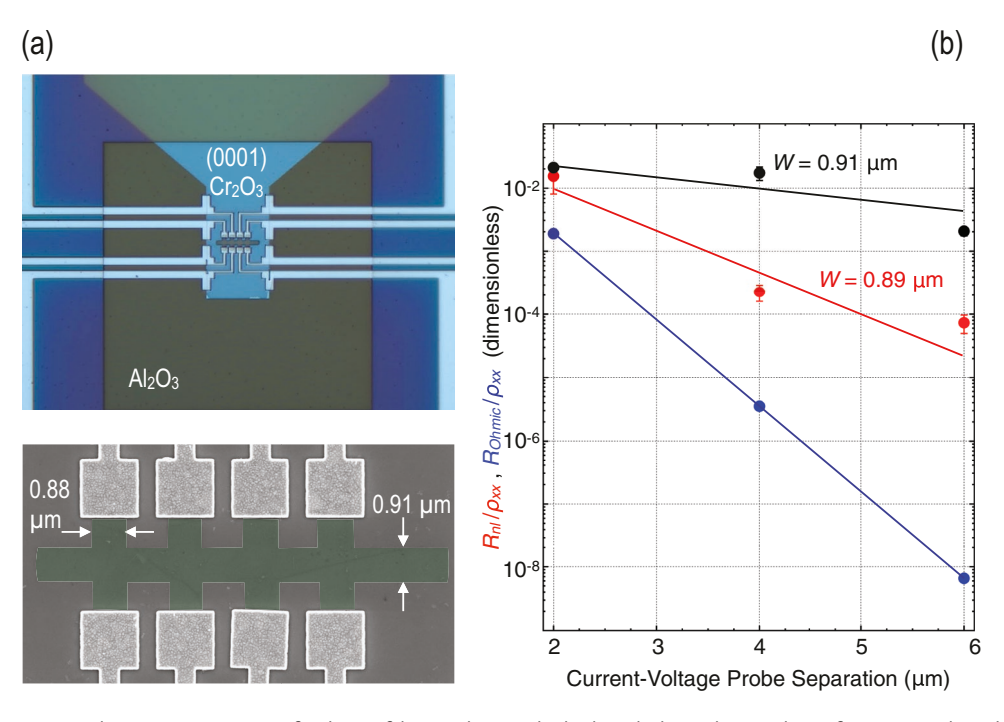


Figure 4. a) Top: 100× optical microscopy image of a device fabricated to study the length-dependent scaling of $R_{\rm nl}$. (Note that, due to the difficulty of observing the graphene on chromia, the image here actually shows the developed PMMA pattern on top of the carbon layer, taken after plasma etching. The PMMA is removed prior to measurement.) The probes are spaced equidistantly along the upper and lower edges of the Hall bar, with a separation between adjacent probes of 2 μm. Current is passed between the leftmost pair of (upper and lower) probes and the non-local voltage drop is measured as in Figure 1b of the main paper. In this way, we are able to measure $R_{\rm nl}$ for a probe separation L=2, 4, and 6 μm. Bottom: Scanning electron microscopy image, taken after the PMMA was removed and all measurements were completed, providing an expanded view of the etched graphene Hall bar (indicated by the use of green false color). b) The red and black symbols show the scaling of $R_{\rm nl}/\rho_{xx}$ with probe separation for two similar devices, fabricated with the geometry shown in (a). Each data point represents an average of $R_{\rm nl}/\rho_{xx}$ obtained while varying back-gate voltage over a range of several volts. The blue data points represent the corresponding contribution of the ohmic resistance, $R_{\rm Ohmic}/\rho_{xx}$ (determined from Equation (1)). The error bars indicated for the non-local resistance represent the measured variation of $R_{\rm nl}/\rho_{xx}$ with gate voltage at each probe separation, while the solid lines are fits to the form of Equation (2). The thickness of the chromia film in these devices was 100 nm.

1521405, 2022, 12, Download from https://olinelibrary.wip.com/doi/10.1002/ahm.202105023 UNCL: University Of Nebraska - Lie Acquisitions Accounting, Wiley Online Library for rules of use; OA articles are governed by the applicable Centive Commons License

where γ is the spin-Hall coefficient (or angle) and is typically in the range of $\approx 0.2-0.6$ when SOC is strong. [27,56] In the main panel of Figure 4b, the red and black data points correspond to the measured variation of R_{nl} for three different probe separations in two different devices (with similar etched widths, as indicated in the figure). Blue data points in the same figure represent the corresponding variation of the ohmic resistance (calculated from the measured resistivity, ρ_{xx} , and the form of Equation (1)). It is clear from this figure that R_{Ohmic} decays much more quickly than R_{nl} , consistent with the truly non-local character of the spin-Hall signal. By fitting the variation of R_{nl} with probe separation to the form of Equation (2), we infer a spin-Hall coefficient γ = 0.5 \pm 0.1 (0.6 \pm 0.2), and a spin relaxation length of $\lambda_s = 2.0 \pm 0.5 \, \mu \text{m} \, (0.7 \pm 0.2 \, \mu \text{m})$ for the black (red) data of Figure 4b. The large value of γ is around twice that reported previously for the giant spin-Hall effect due to residual copper adatoms in CVD grown graphene^[56] and is consistent with strong SOC in our system. It is also clear from a comparison of the data of Figure 4b that the exact magnitude of the non-local signal differs between the two devices. We attribute this to the exponential sensitivity (see Equation (2)) of R_{nl} to differences in the spin-relaxation length; modest changes in the latter parameter, due to microscopic variations in the crystallinity of the CVD graphene, can translate in turn into large changes in R_{nl} .

Finally, there is the issue of the persistence of the non-local spin-Hall signal to temperatures (close to 450 K) well-beyond $T_{\rm N}$. This finding is consistent with results from densityfunctional theory, which have predicted an induced SOC of ≈40 meV in graphene on chromia. [25,26,41] Crucially, our observations confirm that the driving force for this energy scale is the symmetry breaking of the graphene crystal, generated when it is in contact with the chromia. This is not to say that the role of the boundary magnetism, present at the (0001) surface of Cr_2O_3 when $T < T_N$, is unimportant; in this temperature range, it should be possible to exploit the boundary magnetism to reverse the dominant spin species (up or down) in the graphene layer. In this regard, one might consider using B-doped chromia, rather than the intrinsic material that we have used here. Prior work has shown that the Néel temperature of chromia may be raised by B doping, reaching 400 K for a doping content of 3%.[34] Such material should therefore enable the possibility of realizing both robust boundary-magnetism, and strong structurally induced SOC, both well beyond room temperature.

3. Conclusions

We have demonstrated a robust non-local signal, consistent with the spin-Hall effect, in graphene on (0001) $\rm Cr_2O_3$ substrates. While the spin-Hall signal grows with the application of an external magnetic field (normal to the graphene/ $\rm Cr_2O_3$ interface), it nonetheless remains measurable at zero magnetic field. It moreover persists well beyond the Néel temperature of the chromia, to temperatures of at least 450 K. Collectively, our observations point to a strong, externally induced, SOC in graphene, which arises primarily from the influence of the symmetry breaking generated by the $\rm Cr_2O_3$. Our findings are

consistent with the results of calculations based on density functional theory, which predict that this symmetry breaking should generate an effective SOC of ${\approx}40$ meV in the graphene. They moreover suggest that the graphene-on-chromia system should represent an ideal platform for the development of functional spintronic devices, capable of operation at and well-beyond room temperature.

4. Experimental Section

Synthesis of Chromia Films: The single-crystal chromia films used in this work were formed on a layer of (0001) V_2O_3 , which served as a conductive electrode that could be used to back-gate the deposited graphene (see Figure 1b, right panel). The V_2O_3 layer was grown on (0001) α -Al₂O₃ substrates by pulsed laser deposition (PLD), an approach that has previously been shown to support the subsequent growth of high-integrity chromia films. ^[39] After the growth of V_2O_3 , the samples were transferred to a PLD system and held at 700 °C. Chromia was then ablated from a (99.99% pure) ceramic target to deposit a thickness of either 100 or 250 nm. X-ray diffraction confirmed the good (0001) texture achieved in the films, with atomic force microscopy demonstrating their relatively smooth nature (rms roughness \approx 0.2 nm, see Section S1, Supporting Information, for these characterizations).

Fabrication of Graphene-on-(0001)-Chromia Devices: Graphene-on-chromia devices (refer to Figures 1b and 4a) were fabricated by the wet transfer of CVD-grown monolayer graphene (formed on Cu substrates) onto (0001) Cr₂O₃. To prevent cracking and improve adhesion^[59] of the graphene, the transferred samples were annealed for 2 h at 200 °C, under a high vacuum environment (10⁻⁷ Torr). Electrical leakage between the large contact pads of the devices and the conductive^[39] V₂O₃ backelectrode was minimized by depositing a 50 nm layer of Al₂O₃ over most of the graphene/Cr₂O₃ substrate by atomic layer deposition. By leaving a small window without the Al₂O₃ covering, electron-beam lithography and O₂-plasma etching were used to define a graphene Hall bar with the multiprobe geometries shown in Figures 1b and 4a. Electrical contact to the Hall bar was then made by means of an additional electron-beam lithography step, in which 5 nm of Cr and 150 nm of Au were deposited as the contact metals.

Magnetic Characterization of (0001) Chromia: The ME properties of the chromia films were characterized in detail by different methods. [48] These have included measurements of the exchange biasing of Co/Pd multilayers, in which the net boundary magnetism at the (0001) surface of chromia causes a distinct horizontal shift of the former's magnetization curves (see Section S2, Supporting Information, for an example). Detailed temperature-dependent measurements of this effect show [48] that the exchange biasing is lost close to 307 K, consistent with the results of Figure 1c and with the known Néel temperature of chromia. In separate experiments, [48] performed on Pt Hall bars patterned on (0001) Cr₂O₃, it was also shown that a bipolar anomalous Hall signal could be generated by applying voltages of opposite polarity across the chromia. The electrical analogue of the magnetic programming shown in Figure 1c, these measurements collectively establish the well-behaved ME nature of our chromia films.

Electrical Characterization of Graphene-on-(0001)-Chromia Devices: Electrical characteristics of the fabricated devices were measured either by dc (Keithley 2400 source-measure units) or by application of low-frequency (13 Hz) lock-in-detection techniques (Signal Recovery 5210 dual-phase analog lock-in amplifiers). In Section S4 (Supporting Information), results ruling out the possibility of spurious contact effects were presented, by demonstrating that the non-local signal was overwhelmingly symmetric under reversal of the role of the current and voltage contacts. In Section S5 (Supporting Information), a discussion of measurements performed in the presence of an in-plane magnetic field, which is often used as a means to infer spin-dependent transport parameters, was presented. [27]

www.advancedsciencenews.com

www.advmat.de

15214095, 2022, 12, Downloaded from https://onlinelibrary.wiley.com/doi/10.1002/adma.202105023 by UNCL: University Of Nebraska - Line Acquisitions Accounting, Wiley Online Library on [25012023]. See the Terms and Conditions (https://onlinelibrary.wiley.com/doi/10.1002/adma.202105023 by UNCL: University Of Nebraska - Line Acquisitions Accounting, Wiley Online Library on [25012023]. See the Terms and Conditions (https://onlinelibrary.wiley.com/doi/10.1002/adma.202105023 by UNCL: University Of Nebraska - Line Acquisitions Accounting, Wiley Online Library on [25012023]. See the Terms and Conditions (https://onlinelibrary.wiley.com/doi/10.1002/adma.202105023 by UNCL: University Of Nebraska - Line Acquisitions Accounting, Wiley Online Library on [25012023]. See the Terms and Conditions (https://onlinelibrary.wiley.com/doi/10.1002/adma.202105023 by UNCL: University Of Nebraska - Line Acquisitions Accounting, Wiley Online Library on [25012023]. See the Terms and Conditions (https://onlinelibrary.wiley.com/doi/10.1002/adma.202105023 by UNCL: University Of Nebraska - Line Acquisitions Accounting, Wiley Online Library on [25012023]. See the Terms and Conditions (https://onlinelibrary.wiley.com/doi/10.1002/adma.202105023 by UNCL: University Online Library on [25012023]. See the Terms and Conditions (https://onlinelibrary.wiley.com/doi/10.1002/adma.202105023 by UNCL: University Online Library on [25012023]. See the Terms and Conditions (https://onlinelibrary.wiley.com/doi/10.1002/adma.20210502 by UNCL: University Online Library on [25012023]. See the Terms and Conditions (https://onlinelibrary.wiley.com/doi/10.1002/adma.20210502 by UNCL: University Online Library on [25012023]. See the Terms and Conditions (https://onlinelibrary.wiley.com/doi/10.1002/adma.20210502 by UNCL: University Online Library.wiley.com/doi/10.1002/adma.20210502 by UNCL: University Online Library on [25012023]. See the Terms and Conditions (https://onlinelibrary.wiley.com/doi/10.1002/adma.20210502 by UNCL: University Online Library on [25012023]. See t

and-conditions) on Wiley Online Library for rules of use; OA articles are governed by the applicable Creative Commons License

Supporting Information

Supporting Information is available from the Wiley Online Library or from the author.

Acknowledgements

This work was supported by nCORE, a wholly owned subsidiary of the Semiconductor Research Corporation (SRC), through the Center on Antiferromagnetic Magneto-electric Memory and Logic (tasks 2760.001 and 2760.002). Work at Nebraska was also supported by the National Science Foundation, EPSCoR RII Track-1: Emergent Quantum Materials and Technologies (EQUATE), Award OIA-2044049.

Conflict of Interest

The authors declare no conflict of interest.

Data Availability Statement

The data that support the findings of this study are available from the corresponding author upon reasonable request.

Keywords

graphene, non-local transport, spin-Hall effect, spin-orbit coupling, spintronics

Received: June 30, 2021 Revised: December 23, 2021 Published online: February 3, 2022

- [1] S. Datta, B. Das, Appl. Phys. Lett. 1990, 56, 665.
- [2] J. Schliemann, J. C. Egues, D. Loss, Phys. Rev. Lett. 2003, 90, 146801.
- [3] I. Zutic, I. Fabian, S. D. Sarma, Rev. Mod. Phys. 2004, 76, 323.
- [4] Y. G. Semenov, K. W. Kim, J. M. Zavada, Appl. Phys. Lett. 2007, 91, 153105.
- [5] W. Han, R. K. Kawakami, M. Gmitra, J. Fabian, Nat. Nanotechnol. 2014, 9, 794.
- [6] M. V. Kamalakar, C. Groenveld, A. Dankert, S. P. Dash, Nat. Commun. 2015, 6, 6766.
- [7] M. Drögeler, C. Franzen, F. Volmer, T. Pohlmann, L. Banszerus, M. Wolter, K. Watanabe, T. Taniguchi, C. Stampfer, B. Beschoten, Nano Lett. 2016, 16, 3533.
- [8] J. Ingla-Aynés, R. J. Meijerink, B. J. v. Wees, Nano Lett. 2016, 16, 4825.
- [9] W. Yan, L. C. Phillips, M. Barbone, S. J. Hamalainen, A. Lombardo, M. Ghidini, X. Moya, F. Maccherozzi, S. van Dijken, S. S. Dhesi, A. C. Ferrari, N. D. Mathur, *Phys. Rev. Lett.* 2016, 117, 147201.
- [10] J. Panda, M. Ramu, O. Karis, T. Sarkar, M. V. Kamalakar, ACS Nano 2020, 14, 12771.
- [11] Z. M. Gebeyehu, S. Parui, J. F. Sierra, M. Timmermans, M. J. Esplandiu, S. Brems, C. Huyghebaert, K. Garello, M. V. Costache, S. O. Valenzuela, 2D Mater. 2019, 6, 034003.
- [12] I. G. Serrano, J. Panda, F. Denoel, Ö. Vallin, D. Phuyal, O. Karis, M. V. Kamalakar, Nano Lett. 2019, 19, 666.

- [13] H. Min, J. E. Hill, N. A. Sinitsyn, B. R. Sahu, L. Kleinman, A. H. MacDonald, *Phys. Rev. B* **2006**, *74*, 165310.
- [14] S. Konschuh, M. Gmitra, J. Fabian, Phys. Rev. B 2010, 82, 245412.
- [15] O. V. Yazyev, L. Helm, Phys. Rev. B 2007, 75, 125408.
- [16] O. V. Yazyev, Rep. Prog. Phys. 2010, 73, 056501.
- [17] H. Haugen, D. Huertas-Hernando, A. Brataas, Phys. Rev. B 2008, 77, 115406.
- [18] C. Gong, X. Zhang, Science 2019, 363, eaav4450.
- [19] B. Karpiak, A. W. Cummings, K. Zollner, M. Vila, D. Khokhriakov, A. M. Hoque, A. Dankert, P. Svedlindh, J. Fabian, S. Roche, S. P. Dash, 2D Mater. 2019, 7, 015026.
- [20] P. Wei, S. Lee, F. Lemaitre, L. Pinel, D. Cutaia, W. Cha, F. Katmis, Y. Zhu, D. Heiman, J. Hone, J. S. Moodera, C. T. Chen, *Nat. Mater.* 2016, 15, 711.
- [21] D. V. Averyanov, I. S. Sokolov, A. M. Tokmachev, O. E. Parfenov, I. A. Karateev, A. N. Taldenkov, V. G. Storchak, ACS Appl. Mater. Interfaces 2018, 10, 20767.
- [22] C. Tang, Z. Zhang, S. Lai, Q. Tan, W.-B. Gao, Adv. Mater. 2020, 32, 1908498.
- [23] Z. Y. Wang, C. Tang, R. Sachs, Y. Barlas, J. Shi, Phys. Rev. Lett. 2015, 114
- [24] Y.-F. Wu, H.-D. Song, L. Zhang, X. Yang, Z. Ren, D. Liu, H.-C. Wu, J. Wu, J.-G. Li, Z. Jia, B. Yan, X. Wu, C.-G. Duan, G. Han, Z.-M. Liao, D. Yu, Phys. Rev. B 2017, 95, 195426.
- [25] R. Skomski, P. A. Dowben, M. S. Driver, J. A. Kelber, *Mater. Horiz.* 2014, 1, 563.
- [26] S. Cao, Z. Y. Xiao, C. P. Kwan, K. Zhang, J. P. Bird, L. Wang, W. N. Mei, X. Hong, P. A. Dowben, Appl. Phys. Lett. 2017, 111, 182402.
- [27] J. Balakrishnan, G. K. W. Koon, M. Jaiswal, A. H. Castro Neto, B. Özyilmaz, Nat. Phys. 2013, 9, 284.
- [28] S. Y. Zhou, G. H. Gweon, A. V. Fedorov, P. N. First, W. A. de Heer, D. H. Lee, F. Guinea, A. H. Castro Neto, A. Lanzara, *Nat. Mater.* 2007, 6, 770.
- [29] B. Huang, Q. Xu, S.-H. Wei, Phys. Rev. B 2011, 84, 155406.
- [30] S. B. Cho, Y.-C. Chung, J. Mater. Chem. C 2013, 1, 1595.
- [31] G. Giovannetti, P. A. Khomyakov, G. Brocks, P. J. Kelly, J. van den Brink, Phys. Rev. B 2007, 76, 073103.
- [32] N. Sharma, J. P. Bird, C. Binek, P. A. Dowben, D. Nikonov, A. Marshall, Semicond. Sci. Technol. 2020, 35, 073001.
- [33] X. He, Y. Wang, N. Wu, A. N. Caruso, E. Vescovo, K. D. Belashchenko, P. A. Dowben, C. Binek, *Nat. Mater.* 2010, 9, 579
- [34] M. Street, W. Echtenkamp, T. Komesu, S. Cao, P. A. Dowben, C. Binek, Appl. Phys. Lett. 2014, 104, 222402.
- [35] T. Ashida, M. Oida, N. Shimomura, T. Nozaki, T. Shibata, M. Sahashi, Appl. Phys. Lett. 2015, 106, 132407.
- [36] N. Wu, X. He, A. L. Wysocki, U. Lanke, T. Komesu, K. D. Belashchenko, C. Binek, P. A. Dowben, *Phys. Rev. Lett.* 2011, 106, 087202.
- [37] T. Ashida, M. Oida, N. Shimomura, T. Nozaki, T. Shibata, M. Sahashi, Appl. Phys. Lett. 2014, 104, 152409.
- [38] P. A. Dowben, C. Binek, K. Zhang, L. Wang, W. N. Mei, J. P. Bird, U. Singisetti, X. Hong, K. L. Wang, D. Nikonov, *IEEE J. Explor. Solid-State Comput. Devices Circuits* 2018, 4, https://doi.org/10.1109/IXCDC.2018.2809640.
- [39] A. Mahmood, M. Street, W. Echtenkamp, C. P. Kwan, J. P. Bird, C. Binek, *Phys. Rev. Mater.* **2018**, 2, 044401.
- [40] C.-P. Kwan, R. Chen, U. Singisetti, J. P. Bird, Appl. Phys. Lett. 2015, 106, 112901.
- [41] H. Takenaka, S. Sandhoefner, A. A. Kovalev, E. Y. Tsymbal, Phys. Rev. B 2019, 100, 125156.
- [42] H. Yan, Z. Feng, P. Qin, X. Zhou, H. Guo, X. Wang, H. Chen, X. Zhang, H. Wu, C. Jiang, Z. Liu, Adv. Mater. 2020, 32, 1905603.



www.advancedsciencenews.com



www.advmat.de

15214095, 2022, 12, Downloaded from https://onlinelibrary.wiley.com/doi/10.1002/adma.202105023 by UNCL: University Of Nebraska

Linc Acquisitions

Accounting, Wiley Online Library on [25/01/2023]. See the Terms

and-conditions) on Wiley Online Library for rules of use; OA articles are governed by the applicable Creative Commons License

- [43] H.-D. Song, Y.-F. Wu, X. Yang, Z. Ren, X. Ke, M. Kurttepeli, G. V. Tendeloo, D. Liu, H.-C. Wu, B. Yan, X. Wu, C.-G. Duan, G. Han, Z.-M. Liao, D. Yu, Nano Lett. 2018, 18, 2435.
- [44] B. Zhou, J. Balgley, P. Lampen-Kelley, J. Q. Yan, D. G. Mandrus, E. A. Henriksen, *Phys. Rev. B* 2019, 100, 165426.
- [45] Y. Wu, G. Yin, L. Pan, A. J. Grutter, Q. Pan, A. Lee, D. A. Gilbert, J. A. Borchers, W. Ratcliff, A. Li, X.-d. Han, K. L. Wang, Nat. Electron. 2020, 3, 604.
- [46] T. Kosub, M. Kopte, F. Radu, O. G. Schmidt, D. Makarov, Phys. Rev. Lett. 2015, 115, 097201.
- [47] T. Kosub, M. Kopte, R. Hühne, P. Appel, B. Shields, P. Maletinsky, R. Hübner, M. O. Liedke, J. Fassbender, O. G. Schmidt, D. Makarov, Nat. Commun. 2017, 8, 13985.
- [48] J.-L. Wang, W. Echtenkamp, A. Mahmood, C. Binek, J. Magn. Magn. Mater. 2019, 486, 165262.
- [49] Y. Ji, J. Miao, K. K. Meng, Z. Y. Ren, B. W. Dong, X. G. Xu, Y. Wu, Y. Jiang, Appl. Phys. Lett. 2017, 110, 262401.
- [50] R. Schlitz, T. Kosub, A. Thomas, S. Fabretti, K. Nielsch, D. Makarov, S. T. B. Goennenwein, Appl. Phys. Lett. 2018, 112, 132401.

- [51] L. Fallarino, A. Berger, C. Binek, Appl. Phys. Lett. 2014, 104, 022403.
- [52] D. A. Abanin, A. V. Shytov, L. S. Levitov, B. I. Halperin, Phys. Rev. B 2009, 79, 035304.
- [53] G. Mihajlović, J. E. Pearson, M. A. Garcia, S. D. Bader, A. Hoffmann, Phys. Rev. Lett. 2009, 103, 166601.
- [54] J. Renard, M. Studer, J. A. Folk, Phys. Rev. Lett. 2014, 112, 116601.
- [55] M. Ribeiro, S. R. Power, S. Roche, L. E. Hueso, F. Casanova, *Nat. Commun.* 2017, 8, 2198.
- [56] J. Balakrishnan, G. K. W. Koon, A. Avsar, Y. Ho, J. H. Lee, M. Jaiswal, S.-J. Baeck, J.-H. Ahn, A. Ferreira, M. A. Cazalilla, A. H. C. Neto, B. Özyilmaz, *Nat. Commun.* 2014, 5, 4748.
- [57] D. A. Abanin, S. V. Morozov, L. A. Ponomarenko, R. V. Gorbachev, A. S. Mayorov, M. I. Katsnelson, K. Watanabe, T. Taniguchi, K. S. Novoselov, L. S. Levitov, A. K. Geim, *Science* 2011, 332, 328.
- [58] P. Borisov, T. Ashida, T. Nozaki, M. Sahashi, D. Lederman, Phys. Rev. B 2016, 93, 174415.
- [59] X. Liang, B. A. Sperling, I. Calizo, G. Cheng, C. A. Hacker, Q. Zhang, Y. Obeng, K. Yan, H. Peng, Q. Li, X. Zhu, H. Yuan, A. R. H. Walker, Z. Liu, L.-M. Peng, C. A. Richter, ACS Nano 2011, 5, 9144.